



**HAL**  
open science

## Hydrolysis properties, corrosion behavior and microhardness of AZ91 “model” alloys

Serge Al Bacha, Isabelle Aubert, Mirvat Zakhour, Michel Nakhl, Jean-Louis Bobet

► **To cite this version:**

Serge Al Bacha, Isabelle Aubert, Mirvat Zakhour, Michel Nakhl, Jean-Louis Bobet. Hydrolysis properties, corrosion behavior and microhardness of AZ91 “model” alloys. *Journal of Alloys and Compounds*, 2020, 845, 156283 (10 p.). 10.1016/j.jallcom.2020.156283 . hal-02946035

**HAL Id: hal-02946035**

**<https://hal.science/hal-02946035>**

Submitted on 23 Sep 2020

**HAL** is a multi-disciplinary open access archive for the deposit and dissemination of scientific research documents, whether they are published or not. The documents may come from teaching and research institutions in France or abroad, or from public or private research centers.

L'archive ouverte pluridisciplinaire **HAL**, est destinée au dépôt et à la diffusion de documents scientifiques de niveau recherche, publiés ou non, émanant des établissements d'enseignement et de recherche français ou étrangers, des laboratoires publics ou privés.

# Hydrolysis properties, corrosion behavior and microhardness of AZ91 "model" alloys

S. Al Bacha<sup>a,b</sup>, I. Aubert<sup>c</sup>, M. Zakhour<sup>a</sup>, M. Nakhli<sup>a</sup>, J.-L. Bobet<sup>b\*</sup>.

<sup>a</sup> LCPM/PR<sub>2</sub>N (EDST), Lebanese University, Faculty of Sciences II, 90656 Jdeidet El Metn, Lebanon.

<sup>b</sup> University of Bordeaux, ICMCB, UMR 5026, F-33600 Pessac, France.

<sup>c</sup> University of Bordeaux, CNRS, Arts et Metiers Institute of technology, Bordeaux INP, INRAE, I2M Bordeaux, F-33400 Talence, France.

## Abstract

A model AZ91 alloy containing the same amount of Mg and Mg<sub>17</sub>Al<sub>12</sub> than a commercial AZ91 alloy was reproduced using various strategies. These “model” materials consist of a “homemade AZ91” powder, Mg melted or milled with Mg<sub>17</sub>Al<sub>12</sub>. The properties of the various model materials were compared to the commercial alloy (used as reference). The weak bond between Mg and Mg<sub>17</sub>Al<sub>12</sub> is highlighted by SEM observations. Milling Mg with Mg<sub>17</sub>Al<sub>12</sub> enhances the formation of microstructural defects due to the brittleness of the intermetallic. Vickers microhardness of pure Mg<sub>17</sub>Al<sub>12</sub> is 250 Hv while that of AZ91 is 72 Hv. The hardness of Mg<sub>17</sub>Al<sub>12</sub> decreases gradually from the center of the particle to its border in contact with Mg while the hardness of Mg is higher at the interface Mg-Mg<sub>17</sub>Al<sub>12</sub>. The galvanic coupling between Mg and Mg<sub>17</sub>Al<sub>12</sub> improves the hydrolysis performance of the materials. The best hydrolysis performance was 80% of the theoretical capacity of hydrogen production reached in 60 minutes by the milled Mg+Mg<sub>17</sub>Al<sub>12</sub>. The preparation method of the models strongly affects their corrosion behavior. The passivation layer formed during the corrosion of highly-reactive materials affects the electrochemical measurements results. The mechanical properties and the corrosion behavior of the model materials depends on their composition and their structure.

**Keywords:** AZ91, Mg-Al alloys, Mg<sub>17</sub>Al<sub>12</sub>, hydrogen, hardness, corrosion.

\* corresponding author: [jean-louis.bobet@icmcb.cnrs.fr](mailto:jean-louis.bobet@icmcb.cnrs.fr) (J.-L. Bobet)

## 1. Introduction

Corrosion is considered among the main challenges to widen the usage of materials. It is defined as the destruction of the material by a chemical and/or electrochemical reaction with its environment [1]. The degradation is usually accompanied by a loss of the useful properties of the material. Based on the interaction between the material and its environment, the corrosion may be localized or uniform. Localized corrosion reactions are more frequent than uniform corrosion reactions and include: pitting corrosion (studied a lot in chloride solution), crevice corrosion, filiform corrosion, galvanic corrosion, stress corrosion cracking, intergranular corrosion and corrosion fatigue [2]. In this work, we will be focusing on galvanic corrosion since it affects the most the corrosion mechanism of the alloys, which is described as the interaction between different species (*e.g.* metals) in the presence of an electrolyte and an electron conductive path [2, 3]. The electron flow caused by the potential difference favors the oxidation of the more negative potential metal (becomes the anode) while it lowers the corrosion of the more positive potential metal (becomes the cathode) [1]. Many factors affect galvanic corrosion such as the size of the anode and the cathode, the conditions of the aqueous media (*i.e.* composition, temperature, pH, ...), the potential difference and most significantly the surface ratio between the anode and the cathode. From these factors, it is clear that galvanic corrosion occurs at the microstructure scale in multiphase materials as in magnesium-based materials. In these alloys, magnesium (Mg) acts as anode ( $E_{\text{corr}} = -1.65 \text{ V/SCE}$  [4]) while second phases (owing higher open circuit potentials) act as cathodes.

Among all Mg alloys, AZ91 is one of the most popular commercial alloy due to its good mechanical and corrosion resistance properties [5, 6]. The microstructure of AZ91 alloys consists of a primary  $\alpha$  phase (*i.e.* Mg rich), a second  $\beta$ -phase (*i.e.*  $\text{Mg}_{17}\text{Al}_{12}$ ), a binary solid solution  $\text{Mg}_{0.97}\text{Zn}_{0.03}$  and  $\text{Al}_x\text{Mn}_y$  phases [7-17] depending on the solidification and the processing route [18, 19]. In AZ91,  $\text{Mg}_{17}\text{Al}_{12}$ , with an open circuit potential of  $-1.2 \text{ V/SCE}$  [20, 21], acts as a cathode. As the surface ratio between the anode and the cathode influences the galvanic corrosion, the role of  $\text{Mg}_{17}\text{Al}_{12}$  in the corrosion process of AZ91 alloys was evaluated by changing its distribution and morphology in the Mg matrix [5, 19, 22, 23]. It was found that, depending on the surface ratio of  $\text{Mg}_{17}\text{Al}_{12}$  and Mg,  $\beta$ -phase may act as a corrosion barrier or a galvanic cathode [9, 10, 14, 24-26]. However, the corrosion behavior of pure  $\text{Mg}_{17}\text{Al}_{12}$  investigation [27] clarified its role in the

corrosion of AZ alloys where the barrier effect was explained by the lower corrosion kinetics compared to Mg ( $J_{\text{corr}}(\text{Mg}_{17}\text{Al}_{12}) = 5.3 \mu\text{A}/\text{cm}^2$  [27] vs.  $J_{\text{corr}}(\text{Mg}) = 558 \mu\text{A}/\text{cm}^2$  [4]).

Most of the previous studies tended to investigate the corrosion behavior of AZ91 alloys in order to enhance their corrosion resistance. However, the corrosion of Mg-based materials may have some benefits. The oxidation of Mg (during its corrosion) is accompanied by the reduction of water from the aqueous media to produce hydrogen gas ( $\text{H}_2$ ). This reaction is usually reported as the hydrolysis reaction of Mg or Mg-based materials [28-30]. For instance, the hydrolysis reactivity of a material is the same as its anodic dissolution without taking into consideration the negative difference effect (NDE) [31, 32].

Hydrogen production by the hydrolysis/corrosion of AZ91 alloy appears to be an ideal solution for low-cost hydrogen production and for the waste management of Mg-based scrap [7, 33-36]. The reactivity of AZ91 and  $\text{Mg}_{17}\text{Al}_{12}$  was improved by ball milling with cheap additives such as graphite and aluminum chloride [7, 20, 27, 33, 34]. However, the interaction between pure Mg and pure  $\text{Mg}_{17}\text{Al}_{12}$  in the same material is not clear yet. In fact, previous studies explained this interaction based on the variation of their morphology and their distribution.

Besides, the effect of  $\text{Mg}_{17}\text{Al}_{12}$  on the mechanical properties of Mg-Al alloys was also investigated [37-40]. Chowdary *et al.* [38] attributed the highest measured Vickers micro-hardness value, measured on AZ91 sample, to  $\text{Mg}_{17}\text{Al}_{12}$  (133.5 Hv) and the lowest one to Mg (86.3 Hv). When heat treatment was applied on AZ91 alloy, the distribution of  $\text{Mg}_{17}\text{Al}_{12}$  in Mg becomes more homogeneous and as consequence the overall hardness of the alloy was improved [38-40]. The influence of  $\text{Mg}_{17}\text{Al}_{12}$  on the hardness of Mg-Al alloys was highlighted by Sunil *et al.* [37] when comparing the Vickers microhardness of AZ31 and AZ91. In fact, the presence of the brittle  $\text{Mg}_{17}\text{Al}_{12}$  increases the hardness of AZ91 to an average of 110 Hv vs. an average of 85 Hv for AZ31 (note that AZ31 does not contain  $\text{Mg}_{17}\text{Al}_{12}$ , *Cf* reference [37]).

This work attempts to elucidate the effect of  $\text{Mg}_{17}\text{Al}_{12}$  on the corrosion behavior and the hardness of AZ91 alloys. The contribution of the ultra-minority phases  $\text{Mg}_{0.97}\text{Zn}_{0.03}$  and  $\text{Al}_x\text{Mn}_y$  is not considered throughout this study. In an attempt to simulate the contact between Mg and  $\text{Mg}_{17}\text{Al}_{12}$  in AZ91 alloys, three “model” materials and a reference were compared to a commercial AZ91 alloy. The reference consists of a Mg-Al-Zn powder mixture (90:9:1 in wt.%) while the “model”

materials are a homemade AZ91 powder (Mg powder melted with Al and Zn powders, 90:9:1 in wt.%) and a mixture of pure Mg and pure  $Mg_{17}Al_{12}$  synthesized by co-fusion and by ball milling. The results will clarify the role of  $Mg_{17}Al_{12}$  during the hydrolysis/corrosion of Mg-Al alloys offering better understanding on how the hydrolysis of these alloys could be improved. Corrosion behavior (*i.e.* hydrogen production) investigated by anodic polarization, electrochemical impedance spectroscopy and hydrolysis tests will be discussed in terms of microstructural (XRD) and morphological (SEM-EDS, Laser granulometry and Vickers microhardness) analysis.

## 2. Experimental details

### 2.1. Models preparation

Magnesium powder (Strem Chemicals, 99.8%), aluminum powder (Strem Chemicals, 99.7%) and Zinc powder (Prolabo, 99.5%) were used as starting material. “Mg-Al-Zn” was prepared by mixing 90 wt.% of Mg, 9 wt.% of Al and 1 wt.% of Zn in ultrasonic homogenizer in acetone. The mixture was placed into a stainless-steel container and dried for 48h at 373K under Ar atmosphere to get fully rid of air contamination. The same mixture (*i.e.* Mg-Al-Zn) was heated following the temperature program adopted for the synthesis of pure  $Mg_{17}Al_{12}$  [27] to obtain a homemade AZ91 powder (subsequently named AZ91 powder). AZ91 alloy was provided from a local supplier in Bordeaux, France. In order to study the influence of  $Mg_{17}Al_{12}$  on the corrosion behavior of Mg, 78 wt.% of Mg and 21 wt.% of pre-synthesized  $Mg_{17}Al_{12}$  (*i.e.* 90 wt.% of Mg and 10 wt.% of Al) mixtures were synthesized following two procedures: (i) the mixtures was heated at 813K following the temperature program of the synthesis of pure  $Mg_{17}Al_{12}$  [27], hence this material will be named “Mg+ $Mg_{17}Al_{12}$  fusion” and (ii) the mixture was ball milled under Ar for 1h with a rotational speed of 250 rpm following the milling procedure reported previously [7, 27], hence this material will be named “Mg+ $Mg_{17}Al_{12}$  milling”.

## 2.2. Materials characterization

The samples were analyzed by X-ray diffraction (XRD) using a Philips PANalytical X'Pert (PW1820) diffractometer with Cu K $\alpha$ 1 radiation ( $\lambda = 1.5405 \text{ \AA}$ ) for structural characterization and crystalline phases identification. From the XRD refinement using EVA software, Mg crystallite size ( $\tau_{\text{Mg}}$ ) and Mg<sub>17</sub>Al<sub>12</sub> crystallite size ( $\tau_{\text{Mg}_{17}\text{Al}_{12}}$ ) were estimated according to the weighted Scherrer formula. Morphology was observed by scanning electron microscopy (SEM) using a TESCAN VEGA3 SB microscope equipped with a secondary electron detector (SE), a backscattered electron detector (BSE) and an energy dispersive X-ray spectrometer (EDS) for the elemental surface composition analysis. Particle size distribution was evaluated by laser granulometry in absolute ethanol using a MASTERSIZER2000 from Malvern® and results ( $d_{90}$ ; *i.e.* 90% of the particles have a diameter smaller than the represented  $d_{90}$ ) are expressed as number distribution. The Vickers microhardness was measured using a Leica VMHT Auto testing instrument equipped with a pyramidal diamond indenter. An indent force of 1N was applied for 10s on the polished surfaces. The microhardness (Hv) for each sample was estimated using the equation 6.2.6 reported in reference [41]. Average hardness of a minimum of 10 indentations at different regions of the samples is estimated.

## 2.3. Hydrogen production and electrochemical measurements

The hydrolysis performances of the materials were evaluated by monitoring the volume of hydrogen produced over time in a 3.5 wt.% NaCl solution (*i.e.* similar to seawater) [7, 27, 28, 34, 42]. Hydrogen production is presented as the conversion yield (%), which is defined as the volume of produced hydrogen over the theoretical volume of hydrogen calculated using the hydrolysis equation of pure Mg [43] and pure Mg<sub>17</sub>Al<sub>12</sub> [27].

Mg-Al-Zn, Mg+Mg<sub>17</sub>Al<sub>12</sub> fusion and Mg+Mg<sub>17</sub>Al<sub>12</sub> milling were cold-pressed by applying a load of 5500 kg/cm<sup>2</sup> for 3 min to obtain dense pellets with an exposed surface of 0.8 cm<sup>2</sup>. Whereas, AZ91 powder was hot-pressed at 200°C for 30 minutes while applying a load of 500 kg/cm<sup>2</sup> due to the weak bond between Mg and Mg<sub>17</sub>Al<sub>12</sub> [44]. A sample of 0.8 cm<sup>2</sup> was cut from the AZ91

alloy in order to investigate its corrosion behavior and microhardness. All samples were embedded in an insulating resin before electrochemical tests.

Electrochemical measurements (*e.g.* Open Circuit Potential (OCP), anodic polarization curve and Electrochemical Impedance Spectroscopy (EIS)) were performed using an electrochemical workstation (Ametek VersaSTAT 3F type) at room temperature in 3.5 wt.% NaCl solution with a classical three-electrode cell setup [4, 7, 20, 21]. Titanium mesh was used as the counter electrode. All given potentials refer to the saturated calomel electrode (SCE) used as the reference electrode. Before each test, pellets were wet ground with ethanol to a 4000-grit finish. After immersion in NaCl solution for 30 minutes while measuring the OCP, anodic polarization tests were performed by switching the potential to -50 mV/OCP and scanned up to +250 mV/OCP at a scan rate of 0.5 mV/s. The EIS measurements were carried out over a frequency ranging from 100 kHz to 700 mHz with a 10 mV amplitude sinusoidal voltage at OCP after 30 minutes of immersion in the solution. The EIS results were fitted using the commercial ZView 3.5f software. All above electrochemical measurements were repeated at least twice for better reproducibility. The results obtained from the best fit are reported in the present manuscript.

Note that structural analysis, morphological analysis and hydrolysis tests were performed on powders while electrochemical measurements and Vickers hardness tests were achieved on pellets. For AZ91 alloy, hydrolysis tests were made using pellets obtained by face-milling [7].

### **3. Results and discussion**

#### *3.1. AZ91 models characterization*

Figure 1 shows the XRD patterns of Mg-Al-Zn, AZ91 powder, AZ91 alloy, Mg+Mg<sub>17</sub>Al<sub>12</sub> fusion and Mg+Mg<sub>17</sub>Al<sub>12</sub> milling. The Mg<sub>17</sub>Al<sub>12</sub> phase is not observed in Mg-Al-Zn powder since the heating temperature is lower than that needed to form the intermetallic (750K) [27, 45]. However, the other materials are principally composed of approximately 78 wt.% of Mg and 20 wt.% of Mg<sub>17</sub>Al<sub>12</sub> with a minor presence of MgO (2 wt.%).

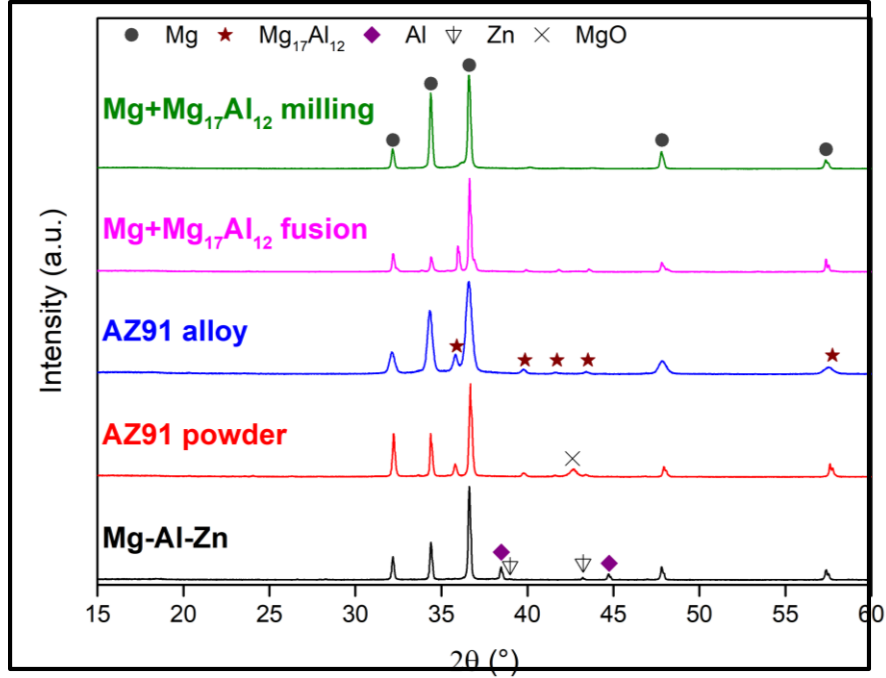


Figure 1: XRD patterns of Mg-Al-Zn, AZ91 powder, AZ91 alloy, Mg+Mg<sub>17</sub>Al<sub>12</sub> fusion and Mg+Mg<sub>17</sub>Al<sub>12</sub> milling.

In an earlier investigation [7], the presence of Mg<sub>0.97</sub>Zn<sub>0.03</sub> in the same AZ91 alloy was highlighted. In the present work, the contribution of this MgZn solid solution in the mechanical properties, the corrosion behavior and the hydrogen generation is considered identical to that of pure Mg. The broadening of the X-ray diffraction peaks is attributed to crystallite size reduction. Mg crystallite size ( $\tau_{\text{Mg}}$ ) decreases from 86 nm for Mg-Al-Zn to an average of 65 nm for the model materials and it shows a minimum of 25 nm for AZ91 alloy (Table 1). The commercial alloy was manufactured at low temperature, which does not favor the growth of Mg crystals. Mg<sub>17</sub>Al<sub>12</sub> crystallite size ( $\tau_{\text{Mg}_{17}\text{Al}_{12}}$ ) shows the highest value (83 nm) for Mg+Mg<sub>17</sub>Al<sub>12</sub> fusion where the pure Mg<sub>17</sub>Al<sub>12</sub> was co-fused with pure Mg without any further treatment (Table 1).  $\tau_{\text{Mg}_{17}\text{Al}_{12}}$  is approximately the same for AZ91 powder and AZ91 alloy (*i.e.*  $\tau_{\text{Mg}_{17}\text{Al}_{12}} = 32$  nm, *Cf* Table 1) and decreases to a minimum of 8 nm for Mg+Mg<sub>17</sub>Al<sub>12</sub> milling as previously reported [27].

Table 1: Mg crystallite size ( $\tau_{Mg}$ ),  $Mg_{17}Al_{12}$  crystallite size ( $\tau_{Mg_{17}Al_{12}}$ ), particle size  $d_{90}$  and Vickers microhardness (HV0.1) of all the materials involved in this study.

Sample	$\tau_{Mg}$ (nm)	$\tau_{Mg_{17}Al_{12}}$ (nm)	Particle size $d_{90}$ ( $\mu m$ )	HV0.1
Mg-Al-Zn	86	-	54	$47 \pm 2$
AZ91 powder	65	32	18	$110 \pm 8$
AZ91 alloy	25	34	Flakes	$72 \pm 2$
Mg+ $Mg_{17}Al_{12}$ fusion	65	83	33	$110 \pm 67$
Mg+ $Mg_{17}Al_{12}$ milling	69	8*	28	$66 \pm 10$

\* the uncertainty on this value is significant but it is indicative that the size of crystallites is very small.

AZ91 powder shows the lowest particle size distribution with a  $d_{90}$  of 18  $\mu m$  (Table 1). During the synthesis of this AZ91 homemade powder, the intermetallic  $Mg_{17}Al_{12}$  is formed and detached from Mg due to the weak bond between them [44]. This explains the low particle size and the fact that AZ91 powder could not be densified by cold-pressing. On the other hand,  $d_{90}$  for Mg+ $Mg_{17}Al_{12}$  milling is lower than that of Mg+ $Mg_{17}Al_{12}$  fusion (*i.e.* 28  $\mu m$  vs. 33  $\mu m$ ) due to the presence of brittle  $Mg_{17}Al_{12}$  [37] during ball milling of Mg which favors particle size reduction.

SEM images (figure 2) were captured via two detectors (*i.e.* BSE and SE) in order to get information about (i) the chemical composition (elucidate the presence of Mg and  $Mg_{17}Al_{12}$ ) with BSE and (ii) surface morphology (by SE).

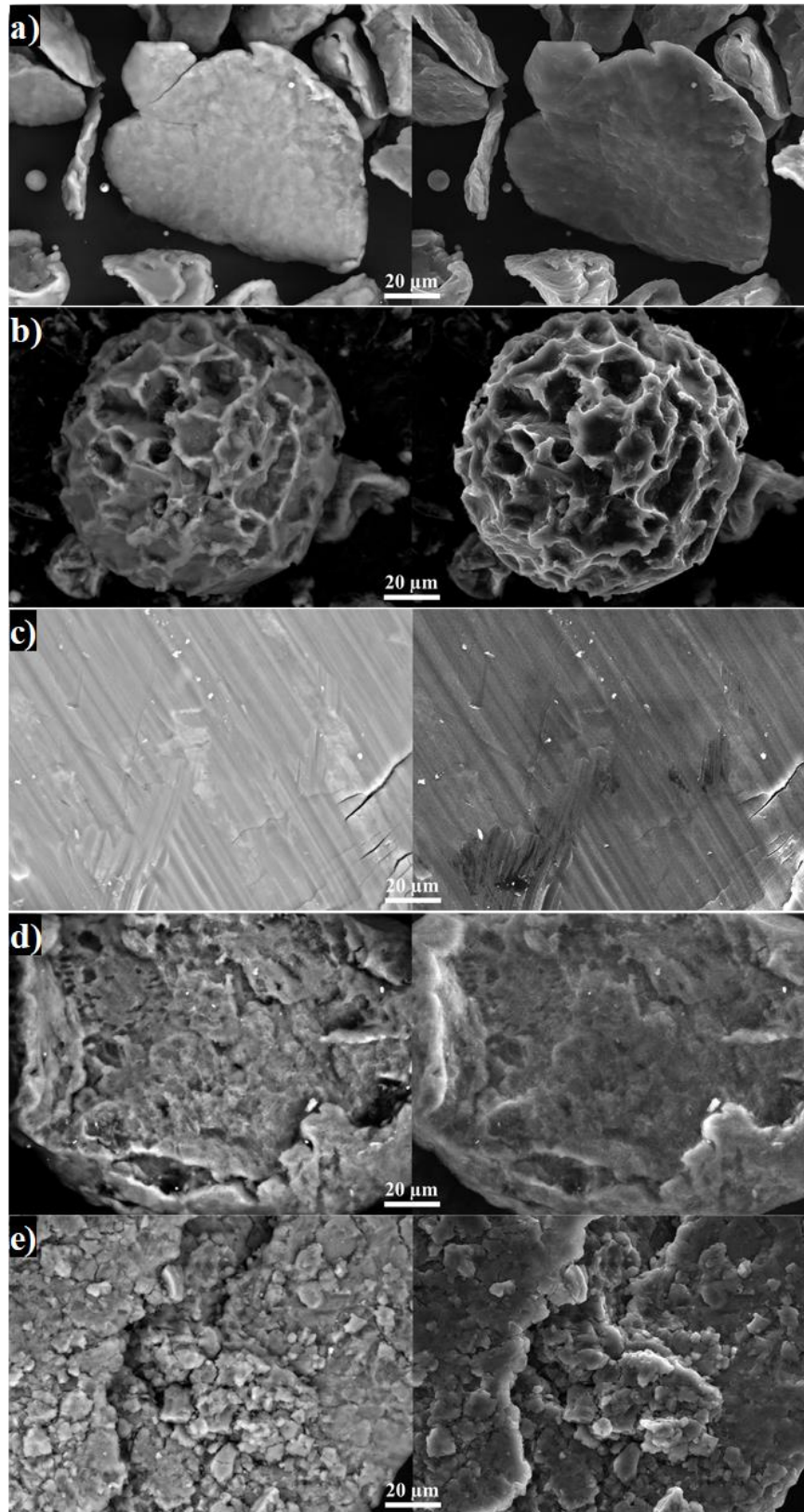


Figure 2: BSE (left) and SE (right) images of a) Mg-Al-Zn, b) AZ91 powder, c) AZ91 alloy, d) Mg+Mg<sub>17</sub>Al<sub>12</sub> fusion and e) Mg+Mg<sub>17</sub>Al<sub>12</sub> milling.

Mg-Al-Zn powders are flat and relatively homogeneous (figure 2.a) whereas AZ91 powder shows particles with a porous structure (figure 2.b). It is possible to attribute this structure to the weak bond between Mg and  $Mg_{17}Al_{12}$  [44] where the formed intermetallic detaches from Mg leaving empty spaces as Raney Nickel (pores of 10  $\mu m$ ). Figure 2.c reveals the presence of  $Mg_{17}Al_{12}$  (white stains) and Mg. When  $Mg_{17}Al_{12}$  is heated with Mg, small fibers type are observed on the surface of Mg+ $Mg_{17}Al_{12}$  fusion (figure 2.d) while Mg+ $Mg_{17}Al_{12}$  shows a rough surface with surface defects (figure 2.e).

Figure 3 highlights the distribution of Mg and Al atoms on the surface of Mg+ $Mg_{17}Al_{12}$  milling where surface defects were formed as shown also in figure 2.e. On overlay of Mg and Al distribution is presented in figure 3 to highlight the presence of  $Mg_{17}Al_{12}$  on the surface of Mg. It is shown that  $Mg_{17}Al_{12}$  forms small particles on the surface and the reduction of  $Mg_{17}Al_{12}$  particle size is accompanied by the formation of microstructural defects (*i.e.* cracks).

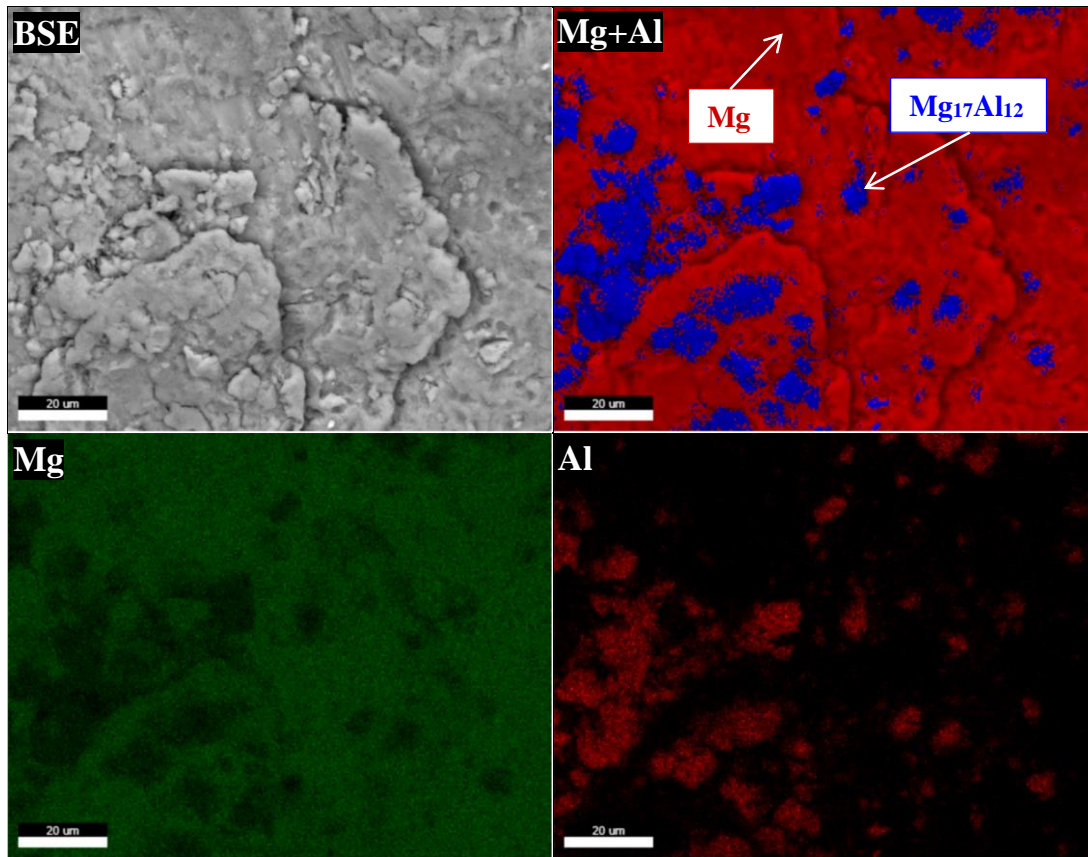


Figure 3: BSE image and EDS mapping of Mg+ $Mg_{17}Al_{12}$  milling.

In order to better understand this microstructure, Vickers microhardness of pure  $Mg_{17}Al_{12}$  was evaluated. Furthermore, the mechanical properties of the models were compared to the commercial alloy.

### 3.2. Vickers hardness

The resistance of a material to a deformation can be quantified by the Vickers microhardness (Hv). The average hardness of pure  $Mg_{17}Al_{12}$  is  $250 \pm 5$  Hv while that of Mg is  $45 \pm 2$  Hv [46, 47]. The hardness of pure  $Mg_{17}Al_{12}$  is higher than that of  $Mg_{17}Al_{12}$  in AZ91 alloy reported by Chowdary *et al.* (*i.e.* 133.5 Hv, *Cf* reference [38]). Table 1 (last left column) shows the mean Vickers hardness for Mg-Al-Zn, AZ91 powder, AZ91 alloys and Mg+ $Mg_{17}Al_{12}$  materials. The reference powder (*i.e.* Mg-Al-Zn) has, as expected, approximately the same hardness as Mg ( $47 \pm 2$  Hv, *Cf* Table 1) since no intermetallic compound is formed. The microhardness of Mg+ $Mg_{17}Al_{12}$  milling is relatively equivalent to that of AZ91 alloy (72 Hv). But the hardness of this alloy is lower than that reported previously and this is probably due to the repartition of  $Mg_{17}Al_{12}$  in the Mg matrix (suggesting that the hardness is expressed only by the rule of mixture [46]). The higher hardness values (*i.e.* 110 Hv) measured for AZ91 powder and Mg+ $Mg_{17}Al_{12}$  fusion indicates an extensive contribution of  $Mg_{17}Al_{12}$  in the mechanical properties of the material. Higher measurement uncertainty is indicative of material heterogeneity especially for Mg+ $Mg_{17}Al_{12}$  fusion.

In order to investigate the mechanical properties of Mg and  $Mg_{17}Al_{12}$  in a “model” AZ91, microhardness indents were carried out by linear scanning on the surface of Mg+ $Mg_{17}Al_{12}$  fusion (Figure 4). The indenter was placed on Mg surface, on  $Mg_{17}Al_{12}$  surface and on a surface containing Mg and  $Mg_{17}Al_{12}$  (Mg,  $Mg_{17}Al_{12}$  and Mg- $Mg_{17}Al_{12}$  in the legend of Figure 4 respectively).

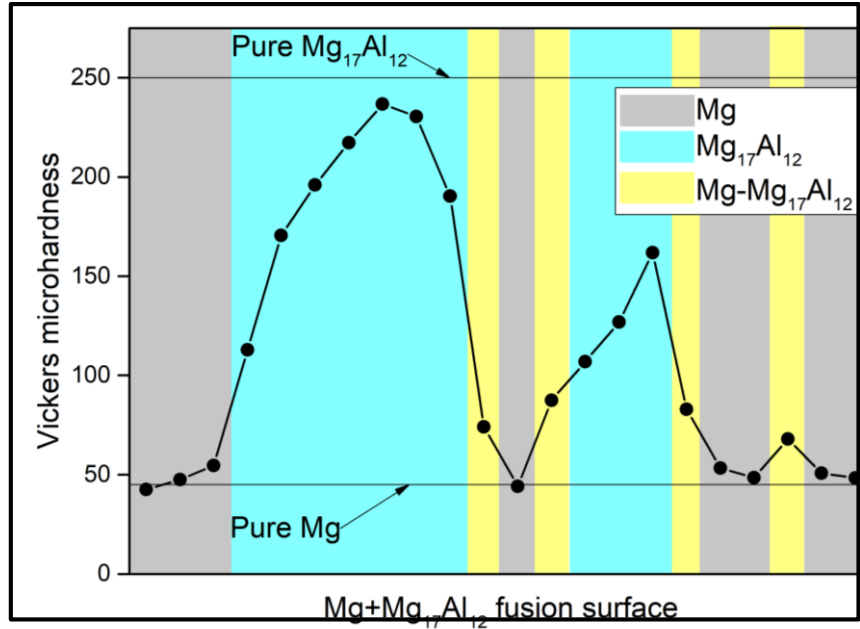


Figure 4: Vickers micro-hardness variation on Mg+Mg<sub>17</sub>Al<sub>12</sub> fusion surface.

Figure 4 shows that the hardness of Mg slightly increases at the interface between Mg and Mg<sub>17</sub>Al<sub>12</sub>. For Mg<sub>17</sub>Al<sub>12</sub>, the hardness increases gradually from the border (the interface between Mg and Mg<sub>17</sub>Al<sub>12</sub>) to the center of the grain. This is a typical composite effect where the weak bond between Mg and Mg<sub>17</sub>Al<sub>12</sub> decreases the hardness of Mg<sub>17</sub>Al<sub>12</sub> in contact with Mg. Based on our results, the lowest value of Mg<sub>17</sub>Al<sub>12</sub> hardness (133.5 Hv [38]) can be explained by the small size of its particles. In other word, the measured hardness was not that of pure Mg<sub>17</sub>Al<sub>12</sub> but was influenced by the Mg matrix. The higher hardness values of Mg-Mg<sub>17</sub>Al<sub>12</sub> materials (compared to pure Mg) offer new perspectives for giving a “second life” as ball milling additive. In fact, milling Mg with AZ91 alloys will induce the formation of surface defects which acts as the initiator sites for the hydrolysis reaction in the presence of Cl<sup>-</sup> ions [2, 48].

### 3.3. Hydrogen production by the hydrolysis reaction

Hydrolysis test of powder were performed in a model seawater solution (*i.e.* 3.5 wt.% of NaCl) using powders. Figure 5 shows that the reactivity, in term of hydrogen generation, varies as follow: Mg+Mg<sub>17</sub>Al<sub>12</sub> milling > AZ91 powder > Mg + Mg<sub>17</sub>Al<sub>12</sub> fusion > Mg-Al-Zn > AZ91 alloy.

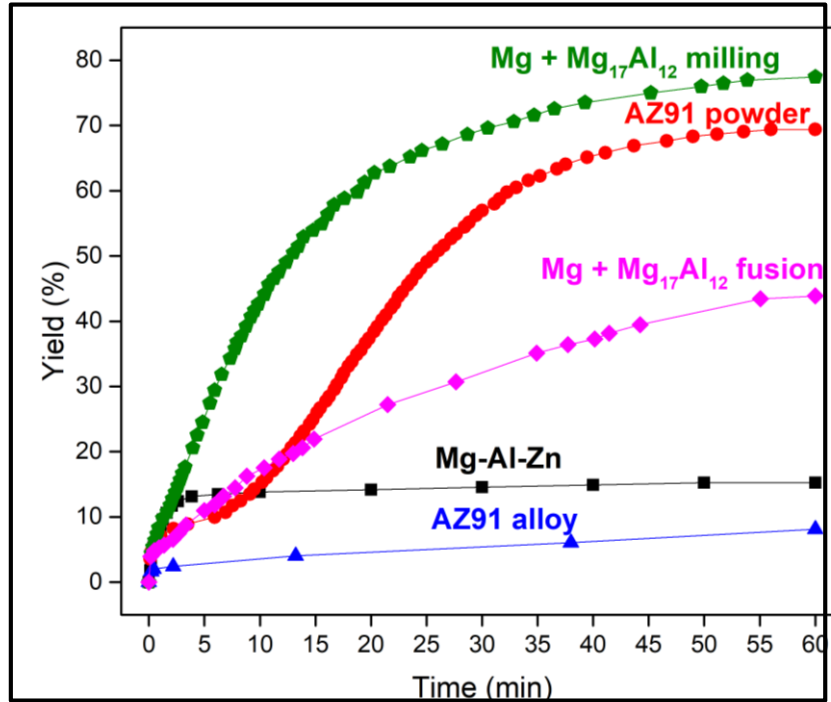


Figure 5: Hydrogen generation of Mg-Al-Zn, AZ91 powder, AZ91 alloy, Mg+Mg<sub>17</sub>Al<sub>12</sub> fusion and Mg+Mg<sub>17</sub>Al<sub>12</sub> milling.

The highest hydrolysis performance (*i.e.* both yield and kinetics) of Mg+Mg<sub>17</sub>Al<sub>12</sub> milling is justified by the establishment of micro-galvanic cells between Mg and Mg<sub>17</sub>Al<sub>12</sub> (as reported between Mg and Ni [28, 30, 48]) and the presence of microstructural defects which enhances the pitting corrosion in the presence of Cl<sup>-</sup> ions [2, 28, 48]. Note that the hydrolysis reaction of AZ91 powder occurs in 2 steps: in the first step (during the first 5 minutes), only Mg reacts with the electrolyte to form Mg(OH)<sub>2</sub> while in the second step (from 5 minutes till the end of the reaction) a magnesium-aluminum hydroxide is formed indicating the contribution of Mg<sub>17</sub>Al<sub>12</sub> in the hydrogen production process. The pellets of AZ91 alloy barely react with a production of 10% of

their theoretical hydrogen production capacity in 60 minutes. The relative low surface area of the pellets does not favor the dissolution of the passivation film of  $\text{Mg}(\text{OH})_2$  formed during the hydrolysis (this phenomenon is well described by the Noyes-Whitney equation [49]).

In order to highlight the effect of  $\text{Mg}_{17}\text{Al}_{12}$  on the hydrolysis performance of Mg, the reactivity of  $\text{Mg}+\text{Mg}_{17}\text{Al}_{12}$  fusion was compared to that of pure Mg and pure  $\text{Mg}_{17}\text{Al}_{12}$  while the performance of  $\text{Mg}+\text{Mg}_{17}\text{Al}_{12}$  milling was compared to milled Mg and milled  $\text{Mg}_{17}\text{Al}_{12}$  (with the same milling conditions). These results are shown in Figures 6.a and 6.b respectively.

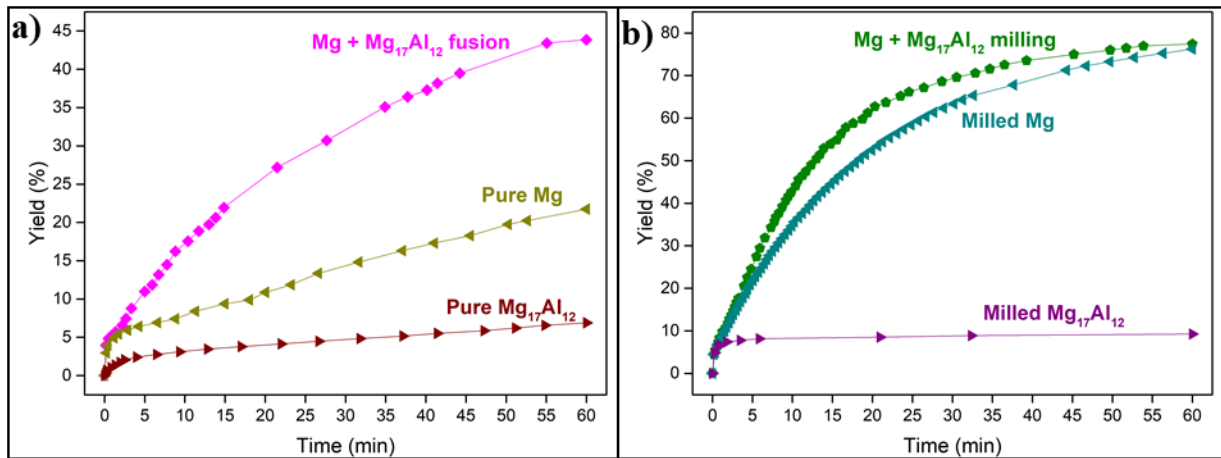


Figure 6: Hydrogen generation of a) pure Mg, pure  $\text{Mg}_{17}\text{Al}_{12}$  and  $\text{Mg}+\text{Mg}_{17}\text{Al}_{12}$  fusion and b) milled Mg, milled  $\text{Mg}_{17}\text{Al}_{12}$  and  $\text{Mg}+\text{Mg}_{17}\text{Al}_{12}$  milling.

Pure  $\text{Mg}_{17}\text{Al}_{12}$  barely reacts with NaCl solution with a generation of 6% of its theoretical  $\text{H}_2$  production capacity in 60 minutes whereas pure Mg produces 20% in the same duration. Conversely, the hydrolysis performances of  $\text{Mg}+\text{Mg}_{17}\text{Al}_{12}$  fusion are better than that of the pure materials with a yield of 43% reached in 60 minutes of reaction. Note that the theoretical hydrogen production capacity by the hydrolysis of  $\text{Mg}+\text{Mg}_{17}\text{Al}_{12}$  materials was calculated by considering the hydrogen production from both Mg and  $\text{Mg}_{17}\text{Al}_{12}$ . Henceforth, the enhancement in the hydrolysis reactivity of  $\text{Mg}+\text{Mg}_{17}\text{Al}_{12}$  fusion is attributed to the galvanic coupling between both compounds, which accelerates the corrosion of the anode (Mg in this case).

On the other hand, ball milling was reported as an efficient method to ameliorate the hydrolysis reactivity of Mg-based materials [50, 51]. In fact, ball milling improves the hydrolysis performance of Mg and Mg<sub>17</sub>Al<sub>12</sub> without exceeding the hydrolysis performance of Mg+Mg<sub>17</sub>Al<sub>12</sub> milling (Figure 6.b). Once again, the better kinetics obtained with Mg+Mg<sub>17</sub>Al<sub>12</sub> milling is attributed to the galvanic coupling. This is attributed to the reduction of the particle size of Mg and Mg<sub>17</sub>Al<sub>12</sub> (promotion of the surface distribution) which increases the contact between the anode and the cathode.

### 3.4. Corrosion behavior

Open Circuit Potential (OCP) for each material involved in this investigation was recorded during 30 minutes of immersion in NaCl solution. Table 2 shows the average OCP values calculated in when the corrosion of the material is in a full steady state (*i.e.* the potential was stable from 15 minutes to 30 minutes of immersion). It is important to point out the difference between two physical values that are very close but different in concept: the OCP and the corrosion potential  $E_{\text{corr}}$ . On the one hand, the OCP is the equilibrium potential between oxidation/reduction of a Mg-based material and it is measured when the material is immersed in electrolyte without applying any potential. On the other hand, the corrosion potential is obtained in similar conditions where cathodic and anodic reactions have the same intensity so that the current at  $E_{\text{corr}}$  is minimal [52]. In the present study, the OCP was estimated when the corrosion of the material is in fully steady state. Consequently, OCP is practically equal to  $E_{\text{corr}}$  (Table 2 and Figure 7.a).

Table 2: OCP values and corrosion current density ( $J_{\text{corr}}$ ) for all the materials involved in this study.

Sample	OCP (V/SCE)	$J_{\text{corr}}$ (mA/cm <sup>2</sup> )
Mg-Al-Zn	-1.63 ± 0.05	4.0 ± 0.1
AZ91 powder	-1.44 ± 0.04	0.35 ± 0.02
AZ91 alloy	-1.63 ± 0.05	0.03 ± 0.001
Mg+Mg <sub>17</sub> Al <sub>12</sub> fusion	-1.62 ± 0.05	9.5 ± 0.4
Mg+Mg <sub>17</sub> Al <sub>12</sub> milling	-1.61 ± 0.05	0.40 ± 0.02

The OCP can be estimated following the rule of mixture [46] by taking into consideration the surface distribution and the OCP of Mg and Mg<sub>17</sub>Al<sub>12</sub>. The structural and morphological dissimilarities (*i.e.* the surface distribution of Mg and Mg<sub>17</sub>Al<sub>12</sub>) between Mg-Al-Zn, AZ91 alloy, Mg+Mg<sub>17</sub>Al<sub>12</sub> fusion and milling didn't affect their corrosion potential (*i.e.* E<sub>corr</sub> of -1.6 V/SCE, Cf Table 2). AZ91 powder exhibits higher OCP value (*e.g.* -1.44 V/SCE); this increase is probably attributed to its smaller particles (implied Mg<sub>17</sub>Al<sub>12</sub>, Cf section 3.1) which increase the surface distribution of Mg<sub>17</sub>Al<sub>12</sub> leading to higher OCP values.

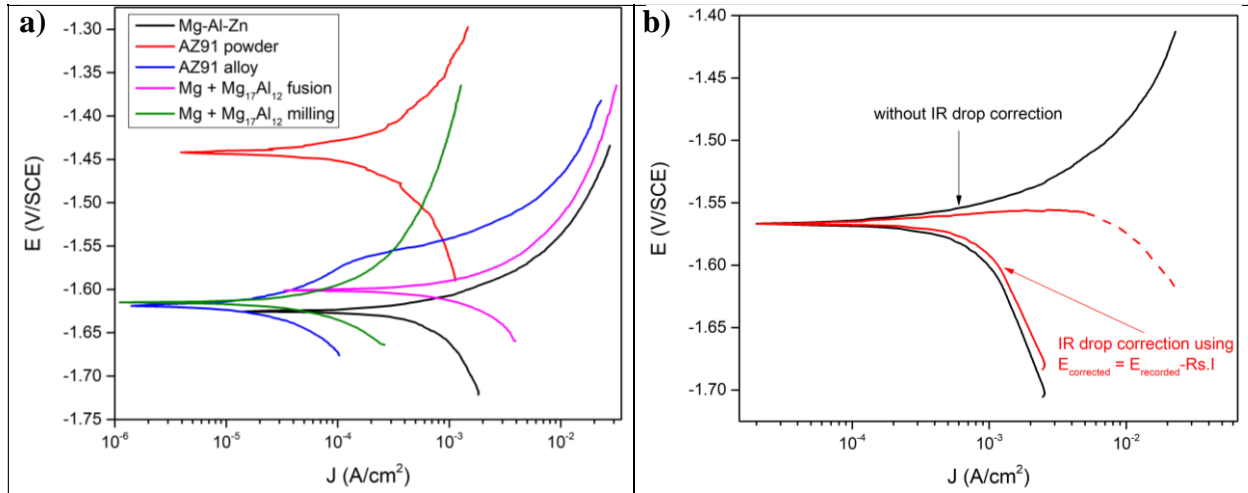


Figure 7: a) Anodic polarization curve for Mg-Al-Zn, AZ91 powder, AZ91 alloy, Mg+Mg<sub>17</sub>Al<sub>12</sub> fusion and Mg+Mg<sub>17</sub>Al<sub>12</sub> milling and b) anodic polarization curve for Mg-Al-Zn obtained after IR drop correction using the relative and the absolute value of the measured current I.

During the polarization of Mg-based materials (Figure 7.a), even with a minimal anodic polarization, a very high anodic current is observed, accompanied by an evolution of hydrogen and a local alkalization [53]. This phenomenon produces the ohmic drop (subsequently named IR drop) in proximity of the working electrode surface and can be corrected according to the equation:

$$E_{\text{corrected}} = E_{\text{recorded}} - R_s \cdot I \quad (1)$$

where E<sub>corrected</sub> and E<sub>recorded</sub> are the applied potential before and after IR drop correction respectively, R<sub>s</sub> is the solution resistance estimated from electrochemical impedance spectroscopy measurements and I is the measured current.

Figure 7.b shows the influence of IR drop correction on the intensity-potential curve obtained for Mg-Al-Zn. The shape of the curves alteration after IR drop correction is attributed to the complicated nature of Mg alloys in anodic polarization state [54, 55] but essentially to the evolution of the solution resistance [53, 56]. In fact,  $R_s$  depends on the applied potential and is strongly affected by the generation of hydrogen bubbles and the local variation of the pH (formation of  $Mg(OH)_2$ ) [56]. Therefore and as recommended by Curioni [56], the anodic polarization results are not corrected for the IR drop. On the other hand, the fact that hydrogen generation is favored with increasing the applied potential during the anodic dissolution of Mg based materials (so that the anodic polarization is not only affected by the anodic reaction) questions the application of Tafel approximation for the estimation of long-term corrosion rates mainly for highly corroding materials [55, 57]. However, we consider that this behavior occurs for all the materials involved in this study.

Corrosion current densities ( $J_{corr}$ ) shown in Table 2 were estimated from the anodic polarization curves presented in Figure 7.a using the method described previously [58, 59]. During anodic corrosion, Mg-Al-Zn and the “model” materials do not reveal the presence of a passivation plateau as observed for the commercial AZ91 alloy (from 0 mV/ $E_{corr}$  to 50 mV/ $E_{corr}$ ). As expected, Mg-Al-Zn powder corrodes faster than the commercial AZ91 alloy known as one of the best corrosion resistant Mg-based alloys ( $J_{corr} = 4 \text{ mA/cm}^2$  for Mg-Al-Zn vs.  $J_{corr} = 0.03 \text{ mA/cm}^2$ , Cf Table 2). The corrosion current density of Mg+Mg<sub>17</sub>Al<sub>12</sub> fusion is greater than that of Mg-Al-Zn powder (4 mA/cm<sup>2</sup>) and AZ91 alloy (0.03 mA/cm<sup>2</sup>) respectively, in total agreement with the results of the hydrolysis tests.

On the other hand, Mg+Mg<sub>17</sub>Al<sub>12</sub> fusion exhibits higher corrosion current densities than Mg+Mg<sub>17</sub>Al<sub>12</sub> milling and AZ91 powder respectively (*i.e.* 0.4 mA/cm<sup>2</sup> and 0.35 mA/cm<sup>2</sup> for Mg+Mg<sub>17</sub>Al<sub>12</sub> milling and AZ91 powder respectively, Cf Table 2). The apparently conflicting results between hydrolysis and anodic polarization come from the fact that hydrolysis allows the study of the reactivity of the whole material while anodic polarization allows to estimate the reactivity of its surface. Therefore, these results are complementary and not contradictory. In fact, low  $J_{corr}$  indicates that the surface of the working electrode is less electrochemically reactive. This decrease is attributed to the formation of thick passivation layer on the surface due to the rapid corrosion during immersion in NaCl solution so that the surface is covered by an insulating material

(considering that AZ91 powder and Mg+Mg<sub>17</sub>Al<sub>12</sub> milling show the best hydrolysis performances, Cf Figure 5). As a consequence, whether the surface is totally or partially covered by the passivation layer, the active surface of Mg decreases which decreases the measured corrosion current, and consequently the corrosion current density drawn in Figure 7.a , which is defined by the ratio between the current and the sample surface. However, if this is the case, the resistance at the interface material-electrolyte should increase due to the presence of an “insulator” and the behavior of the system should be identical to that of a moderately or poorly conductive electrolyte [60]. Indeed, EIS measurements confirms that the solution resistances R<sub>s</sub> (Table 3) are higher for the materials showing the highest hydrolysis performances and the lowest corrosion current densities (*i.e.* AZ91 powder and Mg+Mg<sub>17</sub>Al<sub>12</sub> milling). These findings justify that the passivation layer formed during the corrosion of highly reactive materials affects long-term corrosion rate estimation.

Electrochemical impedance data for all the materials were recorded at OCP after 30 minutes of immersion in NaCl. The experimental data were fitted according to the electrical equivalent circuit adopted previously to explain the effect of ball milling on the corrosion behavior of AZ91 [7, 55]. The equivalent circuit is defined by  $R_s (CPE1 // (R1 (CPE2 // R2)) // (R3L))$  where the parenthesis groups the components connected in series (*e.g.* (R3L)) and the parallel lines (//) represent the components connected in parallel (*e.g.* CPE2//R2). From this circuit, the following EIS parameters are determined: R<sub>s</sub> is the solution resistance, C1 and C2 are the effective capacitances of CPE1 and CPE2 respectively, R<sub>t</sub> the charge transfer resistance and R<sub>p</sub> the polarization resistance [7, 55, 61]. The inductive loop (indicative of the presence of reaction intermediates such as Mg<sup>+</sup> [18, 62-64] or MgH<sup>+</sup> [21]) contribution is expressed by the inductor (L) incorporated in the electrical equivalent circuit [55, 65]. The Nyquist and Bode spectra of the 5 materials in the 3.5 wt.% NaCl solution are depicted in Figure 8.a and Figure 8.b respectively. The experimental data are displayed as scatter plot while the EIS fitting results are represented as line plot.

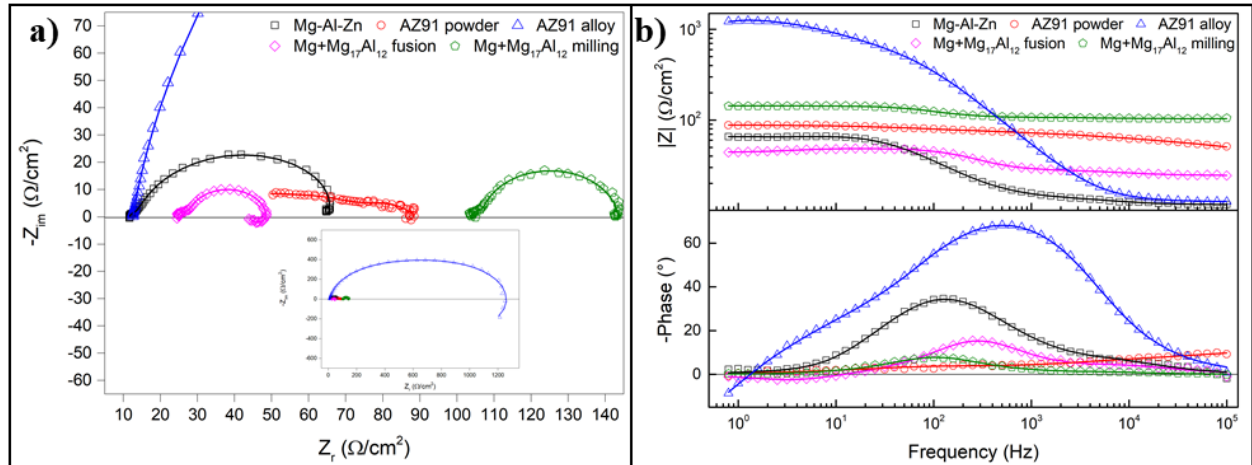


Figure 8: Nyquist (left) and bode (right) plots for Mg-Al-Zn, AZ91 powder, AZ91 alloy, Mg+Mg<sub>17</sub>Al<sub>12</sub> fusion and Mg+Mg<sub>17</sub>Al<sub>12</sub> milling. The inset in Figure 8.a presents the Nyquist plot of AZ91 in 100 kHz – 700 mHz range.

The reference, the commercial alloy and the 3 models have different corrosion behaviors indicating the influence of Mg<sub>17</sub>Al<sub>12</sub> on the corrosion behavior of Mg-Al based materials. The double layer capacitance C1 [55, 65, 66] for AZ91 alloy is lower than that of Mg-Al-Zn, Mg+Mg<sub>17</sub>Al<sub>12</sub> fusion and milling respectively (Table 3). As previously described [7], when corrosion rate increases, the working electrode surface becomes rougher (its surface area increases) and the double layer capacitance increases. For AZ91 powder, the surface impedance distribution (the order of the CPE1) is 0.46 indicating that this CPE1 has no significant physical meaning. It indicates that the corrosion is very fast and that the reaction mechanism is limited by the diffusion [20].

Table 3: Electrochemical parameters calculated from best fit of impedance data of Mg-Al-Zn, AZ91 powder, AZ91 alloy, Mg+Mg<sub>17</sub>Al<sub>12</sub> fusion and Mg+Mg<sub>17</sub>Al<sub>12</sub> milling.

	Mg-Al-Zn	AZ91 powder	AZ91 alloy	Mg+Mg <sub>17</sub> Al <sub>12</sub> fusion	Mg+Mg <sub>17</sub> Al <sub>12</sub> milling
<b>R<sub>s</sub> (Ω/cm<sup>2</sup>)</b>	12	32	13	25	104
<b>C<sub>1</sub> (μF/cm<sup>2</sup>)</b>	13	X	4.7	10	15
<b>C<sub>2</sub> (μF/cm<sup>2</sup>)</b>	63	<b>332</b>	<b>9</b>	51	72
<b>R<sub>t</sub> (Ω/cm<sup>2</sup>)</b>	54	57	1246	24	40
<b>R<sub>p</sub> (Ω/cm<sup>2</sup>)</b>	<b>54</b>	<b>57</b>	<b>700</b>	<b>20</b>	<b>40</b>
<b>R<sub>3</sub> (Ω/cm<sup>2</sup>)</b>	472	225	1372	105	655
<b>L (H/cm<sup>2</sup>)</b>	9	0.001	842	5	0.002

X: C1 value is negligible and it does not have a physical meaning since the surface impedance distribution is 0.46 ( $\approx 0.5$ ) [20].

C<sub>2</sub> characterizes the adsorption pseudo capacitance of corrosion intermediate, corrosion product (*i.e.* Mg(OH)<sub>2</sub>) and/or cathodic reaction initiator sites [55, 67, 68]. Song *et al.* [68] showed that this capacitance increases when species, such as Mg(OH)<sub>2</sub> are adsorbed on the surface. AZ91 shows the lowest C<sub>2</sub> (9 μF/cm<sup>2</sup>) indicating the lowest adsorption of the corrosion product Mg(OH)<sub>2</sub>. On the other side, AZ91 powder shows the highest C<sub>2</sub> value of 332 μF/cm<sup>2</sup>.

The charge transfer resistance R<sub>t</sub> is determined from the EIS Nyquist plot where  $Z_{im} \rightarrow 0 \Omega/cm^2$  (at  $f > 0$  Hz) and the polarization resistance R<sub>p</sub> is estimated for this equivalent circuit according to references [7, 55] (where  $Z_{im} \rightarrow 0 \Omega/cm^2$  at  $f \rightarrow 0$  Hz). Apart AZ91 alloy, R<sub>p</sub> and R<sub>t</sub> are the same for all the other materials due to the less significant contribution of the inductive loop. This suggests that, if a reaction intermediate (*e.g.* Mg<sup>+</sup> or MgH<sup>+</sup>) is formed, it is oxidized to form Mg<sup>2+</sup> without adsorbing on the surface. R<sub>p</sub> is maximal for AZ91 alloy (700 Ω/cm<sup>2</sup>, Cf Table 3) due to the low corrosion rate for the reason that R<sub>p</sub> is inversely proportional to the surface area (while the surface area varies as the corrosion rate) [61]. Nevertheless, Mg+Mg<sub>17</sub>Al<sub>12</sub> fusion exhibits the lowest polarization resistance (*i.e.* 20 Ω/cm<sup>2</sup>, Cf Table 3) indicating the higher corrosion rate. The values of R<sub>p</sub> of AZ91 powder and Mg+Mg<sub>17</sub>Al<sub>12</sub> milling (57 Ω/cm<sup>2</sup> and 40 Ω/cm<sup>2</sup> respectively) comparable to that of Mg-Al-Zn (54 Ω/cm<sup>2</sup>) is attributed to the formation of a thick passivation layer which hinder the corrosion of the bulk material as previously clarified.

## 4. Conclusion

In conclusion, we demonstrated how the manufacturing of Mg-Al alloys (*i.e.* the distribution of Mg and Mg<sub>17</sub>Al<sub>12</sub>) affect the hardness, the hydrolysis performance and the corrosion behavior of the materials. The porous morphology of AZ91 powder proves the weak bond between Mg and Mg<sub>17</sub>Al<sub>12</sub> and results from the leaving phase (Mg<sub>17</sub>Al<sub>12</sub>).

The brittle characteristics of Mg<sub>17</sub>Al<sub>12</sub> were demonstrated. The hardness of pure Mg<sub>17</sub>Al<sub>12</sub> is 5 times higher than that of pure Mg (250 Hv vs. 45 Hv). As a consequence, when Mg<sub>17</sub>Al<sub>12</sub> is used as ball mill additive (*i.e.* Mg+Mg<sub>17</sub>Al<sub>12</sub> milling), particle size is reduced and surface defects (*e.g.* cracks) are formed on Mg surface. On the other hand, the microhardness of Mg<sub>17</sub>Al<sub>12</sub> is influenced by the presence of Mg due to composite effect. For instance, the hardness of Mg<sub>17</sub>Al<sub>12</sub> increases gradually from Mg-Mg<sub>17</sub>Al<sub>12</sub> interface to the center of Mg<sub>17</sub>Al<sub>12</sub> particle.

The comparison of the hydrolysis performance of (i) pure Mg, pure Mg<sub>17</sub>Al<sub>12</sub> and Mg+Mg<sub>17</sub>Al<sub>12</sub> fusion and (ii) milled Mg, milled Mg<sub>17</sub>Al<sub>12</sub> and Mg+Mg<sub>17</sub>Al<sub>12</sub> milling shows the beneficial effect of the galvanic coupling between Mg and Mg<sub>17</sub>Al<sub>12</sub> on the hydrolysis performance of the powder. Mg+Mg<sub>17</sub>Al<sub>12</sub> milling presents the best hydrolysis performance with a yield of 80% of its theoretical hydrogen production capacity reached in 60 minutes of reaction with 3.5 wt.% NaCl aqueous solution. This is probably attributed to the galvanic corrosion and the pitting corrosion favored by the presence of Cl<sup>-</sup> and surface defects in this latter model material. Based on electrochemical test results, the corrosion reactivity is maximal for Mg+Mg<sub>17</sub>Al<sub>12</sub> fusion with the highest corrosion current density ( $J_{\text{corr}} = 9.5 \text{ mA/cm}^2$ ) and lowest polarization resistance ( $R_p = 20 \text{ } \Omega/\text{cm}^2$ ) compared to Mg-Al-Zn ( $J_{\text{corr}} = 4.0 \text{ mA/cm}^2$  and  $R_p = 54 \text{ } \Omega/\text{cm}^2$ ) and AZ91 alloy ( $J_{\text{corr}} = 0.03 \text{ mA/cm}^2$  and  $R_p = 700 \text{ } \Omega/\text{cm}^2$ ).

Hydrolysis and electrochemical tests are generally complementary to evaluate the hydrogen production (the same phenomenon as the anodic corrosion) from Mg-based materials except when the anodic corrosion is very fast. In this case, the thick passivation layer formed hinder the corrosion of the bulk material so that the behavior of the insulating passivation layer is exploited instead of the bulk material.

Our results show that when the particle size of Mg+Mg<sub>17</sub>Al<sub>12</sub> is reduced, the galvanic coupling between Mg and Mg<sub>17</sub>Al<sub>12</sub> is more expressed. It is then worth pointing out that increasing ball milling efficiency of AZ91 until reaching the same powder state as “Mg+Mg<sub>17</sub>Al<sub>12</sub> milling” will improve the hydrogen generation by the hydrolysis reaction. The complete hydrolysis with AZ91 can then be reached by ball milling with additives such aluminum chloride to dissolve the formed Mg(OH)<sub>2</sub>. Moreover, AZ91 alloy can be given a “second life” as ball milling additive due to the fact that it shows a higher microhardness than that of Mg.

## **Acknowledgments**

This work was financially supported by the AZM & SAADE Association, the Lebanese University and Bordeaux foundation. The authors gratefully acknowledge Lionel Teule-Gay for his technical support with Vickers microhardness measurements.

## Highlights

1. Galvanic coupling improves the hydrolysis (corrosion) of AZ alloys.
2. The weak bond between Mg and  $\text{Mg}_{17}\text{Al}_{12}$  was indirectly proved by SEM observations
3. The hardness of  $\text{Mg}_{17}\text{Al}_{12}$  decreases at the interface Mg- $\text{Mg}_{17}\text{Al}_{12}$ .
4. The thick passivation layer formed during the corrosion results in underestimating the corrosion rate by anodic polarization and EIS.

## Bibliography

1. Palit, S., *Recent Advances in Corrosion Science: A Critical Overview and a Deep Comprehension*, in *Direct Synthesis of Metal Complexes*, B. Kharisov, Editor. 2018, Elsevier. p. 379-411.
2. Hamdy Makhoulouf, A.S., *Chapter 15 - Intelligent Stannate-Based Coatings of Self-Healing Functionality for Magnesium Alloys*, in *Intelligent Coatings for Corrosion Control*, A. Tiwari, J. Rawlins, and L.H. Hihara, Editors. 2015, Butterworth-Heinemann: Boston. p. 537-555.
3. Popov, B.N., *Chapter 6 - Galvanic Corrosion*, in *Corrosion Engineering*, B.N. Popov, Editor. 2015, Elsevier: Amsterdam. p. 239-287.
4. Alasmar, E., I. Aubert, A. Durand, M. Nakhl, M. Zakhour, E. Gaudin, and J.L. Bobet, *Hydrogen generation from MgNdNiMg15 composites by hydrolysis reaction*. International Journal of Hydrogen Energy, 2019. **44**(2): p. 523-530.
5. Zhao, Y.-C., M.-C. Zhao, R. Xu, L. Liu, J.-X. Tao, C. Gao, C. Shuai, and A. Atrens, *Formation and characteristic corrosion behavior of alternately lamellar arranged  $\alpha$  and  $\beta$  in as-cast AZ91 Mg alloy*. Journal of Alloys and Compounds, 2019. **770**: p. 549-558.
6. Rocca, E., C. Juers, and J. Steinmetz, *Corrosion behaviour of chemical conversion treatments on as-cast Mg–Al alloys: Electrochemical and non-electrochemical methods*. Corrosion Science, 2010. **52**(6): p. 2172-2178.
7. Al Bacha, S., I. Aubert, M. Zakhour, M. Nakhl, and J.L. Bobet, *Hydrogen production by the hydrolysis of ball milled AZ91 (Electrochemical approach)*. Submitted to Journal of Power Sources, 2020.
8. Dargusch, M.S., M. Nave, S.D. McDonald, and D.H. StJohn, *The effect of aluminium content on the eutectic morphology of high pressure die cast magnesium–aluminium alloys*. Journal of Alloys and Compounds, 2010. **492**(1): p. L64-L68.
9. Song, G., A. Atrens, X. Wu, and B. Zhang, *Corrosion behaviour of AZ21, AZ501 and AZ91 in sodium chloride*. Corrosion Science, 1998. **40**(10): p. 1769-1791.
10. Song, G., A. Atrens, and M. Dargusch, *Influence of microstructure on the corrosion of diecast AZ91D*. Corrosion Science, 1998. **41**(2): p. 249-273.
11. Lunder, O., J.E. Lein, T.K. Aune, and K. Nisancioglu, *The Role of Mg17Al12 Phase in the Corrosion of Mg Alloy AZ91*. CORROSION, 1989. **45**(9): p. 741-748.
12. Singh, I.B., M. Singh, and S. Das, *A comparative corrosion behavior of Mg, AZ31 and AZ91 alloys in 3.5% NaCl solution*. Journal of Magnesium and Alloys, 2015. **3**(2): p. 142-148.

13. Bland, L.G., L.C. Scully, and J.R. Scully, *Assessing the Corrosion of Multi-Phase Mg-Al Alloys with High Al Content by Electrochemical Impedance, Mass Loss, Hydrogen Collection, and Inductively Coupled Plasma Optical Emission Spectrometry Solution Analysis*. CORROSION, 2017. **73**(5): p. 526-543.
14. Feng, H., S. Liu, Y. Du, T. Lei, R. Zeng, and T. Yuan, *Effect of the second phases on corrosion behavior of the Mg-Al-Zn alloys*. Journal of Alloys and Compounds, 2017. **695**: p. 2330-2338.
15. Wen, Z., C. Wu, C. Dai, and F. Yang, *Corrosion behaviors of Mg and its alloys with different Al contents in a modified simulated body fluid*. Journal of Alloys and Compounds, 2009. **488**(1): p. 392-399.
16. Chen, J., J. Wang, E. Han, J. Dong, and W. Ke, *States and transport of hydrogen in the corrosion process of an AZ91 magnesium alloy in aqueous solution*. Corrosion Science, 2008. **50**(5): p. 1292-1305.
17. Woo, S.K., C. Blawert, K.A. Yasakau, S. Yi, N. Scharnagl, B.-C. Suh, Y.M. Kim, B. Sun You, and C. Dong Yim, *Effects of combined addition of Ca and Y on the corrosion behaviours of die-cast AZ91D magnesium alloy*. Corrosion Science, 2020. **166**: p. 108451.
18. Esmaily, M., J.E. Svensson, S. Fajardo, N. Birbilis, G.S. Frankel, S. Virtanen, R. Arrabal, S. Thomas, and L.G. Johansson, *Fundamentals and advances in magnesium alloy corrosion*. Progress in Materials Science, 2017. **89**: p. 92-193.
19. Zhang, Z., G. Wu, A. Atrens, and W. Ding, *Influence of trace As content on the microstructure and corrosion behavior of the AZ91 alloy in different metallurgical conditions*. Journal of Magnesium and Alloys, 2020.
20. Al Bacha, S., I. Aubert, O. Devos, M. Zakhour, M. Nakhl, and J.L. Bobet, *Corrosion behavior of pure Mg<sub>17</sub>Al<sub>12</sub> and effect of ball milling in presence of additives (Graphite and MgCl<sub>2</sub>)*. International Journal of Hydrogen Energy, 2020. **45**(32): p. 15805-15813.
21. Al Bacha, S., A. Desmedt, and J.L. Bobet, *Experimental evidence of H<sub>2</sub> spillover during the corrosion of Mg<sub>17</sub>Al<sub>12</sub>*. Submitted to Corrosion Science, 2020.
22. Zhao, M.-C., M. Liu, G. Song, and A. Atrens, *Influence of the  $\beta$ -phase morphology on the corrosion of the Mg alloy AZ91*. Corrosion Science, 2008. **50**(7): p. 1939-1953.
23. Zhao, M.C., M. Liu, G.L. Song, and A. Atrens, *Influence of Homogenization Annealing of AZ91 on Mechanical Properties and Corrosion Behavior*. Advanced Engineering Materials, 2008. **10**(1 - 2): p. 93-103.
24. Cheng, Y.-l., T.-w. Qin, H.-m. Wang, and Z. Zhang, *Comparison of corrosion behaviors of AZ31, AZ91, AM60 and ZK60 magnesium alloys*. Transactions of Nonferrous Metals Society of China, 2009. **19**(3): p. 517-524.

25. Zhao, M.C., P.J. Uggowitzer, M. Liu, P. Schmutz, G. Song, and A. Atrens, *Corrosion of AZ91 - Influence of the  $\beta$ -Phase Morphology*. Materials Science Forum, 2009. **618-619**: p. 473-478.
26. Büttev Öcal, E., Z. Esen, K. Aydınol, and A.F. Dericioğlu, *Comparison of the short and long-term degradation behaviors of as-cast pure Mg, AZ91 and WE43 alloys*. Materials Chemistry and Physics, 2020. **241**: p. 122350.
27. Al Bacha, S., M. Zakhour, M. Nakhl, and J.L. Bobet, *Effect of ball milling in presence of additives (Graphite,  $AlCl_3$ ,  $MgCl_2$  and  $NaCl$ ) on the hydrolysis performances of  $Mg_{17}Al_{12}$* . International Journal of Hydrogen Energy, 2020. **45**(11): p. 6102-6109.
28. Al Bacha, S., A.S. Awad, E. El Asmar, T. Tayeh, J.L. Bobet, M. Nakhl, and M. Zakhour, *Hydrogen generation via hydrolysis of ball milled WE43 magnesium waste*. International Journal of Hydrogen Energy, 2019. **44**(33): p. 17515-17524.
29. Alasmar, E., A.S. Awad, D. Hachem, T. Tayeh, M. Nakhl, M. Zakhour, E. Gaudin, and J.L. Bobet, *Hydrogen generation from Nd-Ni-Mg system by hydrolysis reaction*. Journal of Alloys and Compounds, 2018. **740**: p. 52-60.
30. Awad, A.S., E. El-Asmar, T. Tayeh, F. Mauvy, M. Nakhl, M. Zakhour, and J.L. Bobet, *Effect of carbons (G and CFs), TM (Ni, Fe and Al) and oxides ( $Nb_2O_5$  and  $V_2O_5$ ) on hydrogen generation from ball milled Mg-based hydrolysis reaction for fuel cell*. Energy, 2016. **95**: p. 175-186.
31. Zhang, W., Q. Liu, Y. Chen, and G. Wan, *Anodic dissolution dictates the negative difference effect (NDE) of magnesium corrosion more in chemical pathway*. Materials Letters, 2018. **232**: p. 54-57.
32. Thomaz, T.R., C.R. Weber, T. Pelegrini, L.F.P. Dick, and G. Knörnschild, *The negative difference effect of magnesium and of the AZ91 alloy in chloride and stannate-containing solutions*. Corrosion Science, 2010. **52**(7): p. 2235-2243.
33. S. Al Bacha, P.S.A., Urretavizcaya, G., M. Zakhour, F.J. Castro, M. Nakhl, J.-L. Bobet, *Effect of ball milling strategy on the hydrolysis performance of Mg alloy waste*. Accepted in the International Journal of Hydrogen Energy, 2020.
34. S. Al Bacha, P.S.A., Urretavizcaya, G., M. Zakhour, F.J. Castro, M. Nakhl, J.-L. Bobet, *Hydrogen generation from ball milled Mg alloy waste by hydrolysis reaction*. Submitted to Journal of Power Sources, 2020.
35. Uan, J.-Y., M.-C. Lin, C.-Y. Cho, K.-T. Liu, and H.-I. Lin, *Producing hydrogen in an aqueous NaCl solution by the hydrolysis of metallic couples of low-grade magnesium scrap and noble metal net*. International Journal of Hydrogen Energy, 2009. **34**(4): p. 1677-1687.
36. Uan, J.-Y., S.-H. Yu, M.-C. Lin, L.-F. Chen, and H.-I. Lin, *Evolution of hydrogen from magnesium alloy scraps in citric acid-added seawater without catalyst*. International Journal of Hydrogen Energy, 2009. **34**(15): p. 6137-6142.

37. Sunil, B.R., K.V. Ganesh, P. Pavan, G. Vadapalli, C. Swarnalatha, P. Swapna, P. Bindukumar, and G. Pradeep Kumar Reddy, *Effect of aluminum content on machining characteristics of AZ31 and AZ91 magnesium alloys during drilling*. Journal of Magnesium and Alloys, 2016. **4**(1): p. 15-21.
38. V, S.C., R. Dumpala, A.K. S, K. Vv, and R.S. B, *Influence of heat treatment on the machinability and corrosion behavior of AZ91 Mg alloy*. Journal of Magnesium and Alloys, 2018. **6**(1): p. 52-58.
39. Xu, S.W., N. Matsumoto, S. Kamado, T. Honma, and Y. Kojima, *Effect of Mg17Al12 precipitates on the microstructural changes and mechanical properties of hot compressed AZ91 magnesium alloy*. Materials Science and Engineering: A, 2009. **523**(1): p. 47-52.
40. Lee, J.U., S.-H. Kim, Y.J. Kim, and S.H. Park, *Effects of homogenization time on aging behavior and mechanical properties of AZ91 alloy*. Materials Science and Engineering: A, 2018. **714**: p. 49-58.
41. *Chapter 6 - Evaluation methods for properties of nanostructured body*, in *Nanoparticle Technology Handbook (Second Edition)*, M. Hosokawa, et al., Editors. 2012, Elsevier: Amsterdam. p. 317-383.
42. Tayeh, T., A.S. Awad, M. Nakhl, M. Zakhour, J.F. Silvain, and J.L. Bobet, *Production of hydrogen from magnesium hydrides hydrolysis*. International Journal of Hydrogen Energy, 2014. **39**(7): p. 3109-3117.
43. Xiao, F., Y. Guo, R. Yang, and J. Li, *Hydrogen generation from hydrolysis of activated magnesium/low-melting-point metals alloys*. International Journal of Hydrogen Energy, 2019. **44**(3): p. 1366-1373.
44. Tolouie, E. and R. Jamaati, *Effect of  $\beta$ -Mg17Al12 phase on microstructure, texture and mechanical properties of AZ91 alloy processed by asymmetric hot rolling*. Materials Science and Engineering: A, 2018. **738**: p. 81-89.
45. Monas, A., O. Shchyglo, S.-J. Kim, C.D. Yim, D. Höche, and I. Steinbach, *Divorced Eutectic Solidification of Mg-Al Alloys*. JOM, 2015. **67**(8): p. 1805-1811.
46. Alasmar, E., *Systèmes ternaires à base de magnésium : synthèse, structure, propriétés physiques, stockage et/ou production d'hydrogène*. 2018.
47. Revie, R.W., *Uhlig's corrosion handbook*. Vol. 51. 2011: John Wiley & Sons.
48. Grosjean, M.H., M. Zidoune, and L. Roué, *Hydrogen production from highly corroding Mg-based materials elaborated by ball milling*. Journal of Alloys and Compounds, 2005. **404-406**: p. 712-715.
49. Hattori, Y., Y. Haruna, and M. Otsuka, *Dissolution process analysis using model-free Noyes–Whitney integral equation*. Colloids and Surfaces B: Biointerfaces, 2013. **102**: p. 227-231.

50. Grosjean, M.-H., M. Zidoune, L. Roué, J. Huot, and R. Schulz, *Effect of ball milling on the corrosion resistance of magnesium in aqueous media*. *Electrochimica Acta*, 2004. **49**(15): p. 2461-2470.
51. Xie, X., C. Ni, B. Wang, Y. Zhang, X. Zhao, L. Liu, B. Wang, and W. Du, *Recent advances in hydrogen generation process via hydrolysis of Mg-based materials: A short review*. *Journal of Alloys and Compounds*, 2020. **816**: p. 152634.
52. Zhang, X.G., *Corrosion Potential and Corrosion Current*, in *Corrosion and Electrochemistry of Zinc*. 1996, Springer US: Boston, MA. p. 125-156.
53. Curioni, M., F. Scenini, T. Monetta, and F. Bellucci, *Correlation between electrochemical impedance measurements and corrosion rate of magnesium investigated by real-time hydrogen measurement and optical imaging*. *Electrochimica Acta*, 2015. **166**: p. 372-384.
54. Cui, Z., F. Ge, Y. Lin, L. Wang, L. Lei, H. Tian, M. Yu, and X. Wang, *Corrosion behavior of AZ31 magnesium alloy in the chloride solution containing ammonium nitrate*. *Electrochimica Acta*, 2018. **278**: p. 421-437.
55. King, A.D., N. Birbilis, and J.R. Scully, *Accurate Electrochemical Measurement of Magnesium Corrosion Rates; a Combined Impedance, Mass-Loss and Hydrogen Collection Study*. *Electrochimica Acta*, 2014. **121**: p. 394-406.
56. Curioni, M., *The behaviour of magnesium during free corrosion and potentiodynamic polarization investigated by real-time hydrogen measurement and optical imaging*. *Electrochimica Acta*, 2014. **120**: p. 284-292.
57. Shi, Z., M. Liu, and A. Atrens, *Measurement of the corrosion rate of magnesium alloys using Tafel extrapolation*. *Corrosion Science*, 2010. **52**(2): p. 579-588.
58. Jayaraj, J., S. Amruth Raj, A. Srinivasan, S. Ananthakumar, U.T.S. Pillai, N.G.K. Dhaipule, and U.K. Mudali, *Composite magnesium phosphate coatings for improved corrosion resistance of magnesium AZ31 alloy*. *Corrosion Science*, 2016. **113**: p. 104-115.
59. Zheng, T., Y. Hu, F. Pan, Y. Zhang, and A. Tang, *Fabrication of corrosion-resistant superhydrophobic coating on magnesium alloy by one-step electrodeposition method*. *Journal of Magnesium and Alloys*, 2019. **7**(2): p. 193-202.
60. Chechirlian, S., *Contribution à l'étude électrochimique de la corrosion dans les milieux à faible conductivité : application à l'étude du comportement d'aciers inoxydables austénitiques dans les solutions concentrées d'acide acétique*. 1989. p. 1 vol. (218 p.).
61. Córdoba-Torres, P., *Relationship between constant-phase element (CPE) parameters and physical properties of films with a distributed resistivity*. *Electrochimica Acta*, 2017. **225**: p. 592-604.
62. Klotz, D., *Negative capacitance or inductive loop? – A general assessment of a common low frequency impedance feature*. *Electrochemistry Communications*, 2019. **98**: p. 58-62.

63. Dobbelaar, J.A.L. and J.H.W. de Wit, *Impedance Measurements and Analysis of the Corrosion of Chromium*. Journal of The Electrochemical Society, 1990. **137**(7): p. 2038-2046.
64. Bender, S., J. Goellner, A. Heyn, and S. Schmigalla, *A new theory for the negative difference effect in magnesium corrosion*. Materials and Corrosion, 2012. **63**(8): p. 707-712.
65. Orazem, M.E. and B. Tribollet, *Electrochemical impedance spectroscopy*. 2017: John Wiley & Sons.
66. Agarwal, P., *Measurement Models for Electrochemical Impedance Spectroscopy*. Journal of The Electrochemical Society, 1992. **139**(7): p. 1917.
67. Murray, J.N., P.J. Moran, and E. Gileadi, *Utilization of the Specific Pseudocapacitance for Determination of the Area of Corroding Steel Surfaces*. CORROSION, 1988. **44**(8): p. 533-538.
68. Song, G. and D. StJohn, *Corrosion behaviour of magnesium in ethylene glycol*. Corrosion Science, 2004. **46**(6): p. 1381-1399.